

Chapter 2

Radiation Properties of Edge-Coupled Split-Ring Resonators (EC-SRRs) and Derived Structures

In this chapter, a study of the radiation properties of the SRR and other metamaterial-inspired resonators will be detailed. Due to its uniplanar geometry, which contributed to its widespread diffusion in the metamaterial community, the edge-coupled SRR (EC-SRR) is the topology considered throughout this work. Analytical approach was at the base of the presented results, and provided approximated expressions for the most relevant antenna parameters, such as the input resistance, the radiation efficiency and the cross-polarization of the radiated fields. The results have been validated by comparison with full-wave EM simulations in different cases, obtaining good agreement.

The expressions obtained in this chapter are at the base of the antenna designs presented in the next chapter, where experimental data provided additional validation of the analysis exposed below.

2.1 EC-SRR at Its Fundamental Resonance

The topology of the EC-SRR is depicted in Fig. 2.1 (cylindrical coordinate system r, z, φ is adopted for the analysis). The ring trace width, c , is assumed to be the same for both rings, a condition which is usually complied in most of the designs involving the EC-SRR. The width of the cuts in each ring is not critical for the SRR response, since the capacitance associated to the cut can be neglected [1]. Its value is set greater than the distance between rings d and, obviously, much smaller than the mean ring radius $r_0 = (r_A + r_B)/2$, where r_A and r_B are the mean radii of the external and internal rings, respectively.

The electric current distribution in each ring at the fundamental (first) resonance can be found from the quasi-static analysis presented in [2], which assumes that the particle length is small in terms of wavelengths. Such assumption is usually satisfied in practical SRR designs, where the coupling between the internal and external rings makes the resonant particle much smaller than the wavelength,

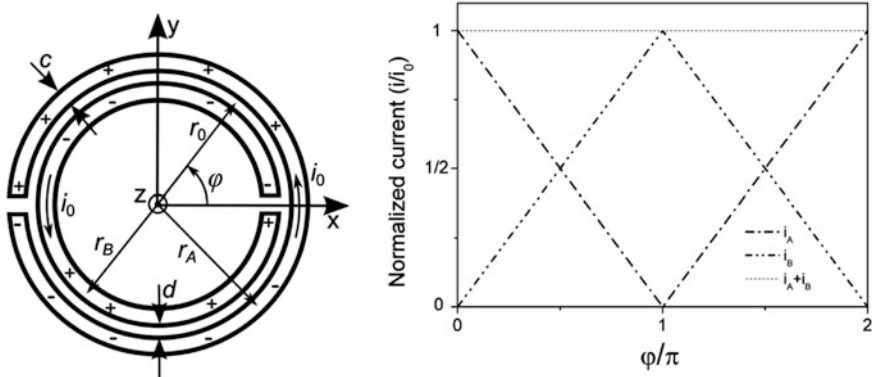


Fig. 2.1 Topology and electric current/charge distribution of the EC-SRR at its fundamental resonance under the quasi-static approximation

typically in the order of $\lambda_0/10$ (in terms of diameter) [3], where λ_0 is the free-space wavelength. Strong coupling between rings involves a reasonably small distance d between rings, which ensure a high value of distributed capacitance between rings. From the quasi-static analysis, it was found that: (i) the currents on the internal and external rings flow in the same direction, and present the same maximum amplitude i_0 , (ii) the current on each ring can be approximated to follow a linear dependence over the position angle φ , (iii) the current at the ring cuts is approximately zero, since the capacitance associated to the cuts in each ring can be neglected. Due to the considerations above and the position of the cuts, the sum of the currents in the outer and inner rings is constant and equal to i_0 along the whole circumference (it does not depend on the position angle φ), as represented in Fig. 2.1. Hence, it follows that the SRR can be treated like a constant current loop of radius r_0 in terms of magnetic polarizability. This has been usually done in the quasi-static analysis of the particle, in order to evaluate its magnetic polarizability around the resonance [3]. However, while this approach is a good approximation for typical EC-SRR designs (where $c \ll r_0$), SRR designs oriented to radiation require a more accurate analysis. This is because, in order to obtain high radiation efficiency, the rings of a radiating SRR are required to be somewhat wider (see Sect. 2.1.2), as compared to the rings of an SRR used in metamaterial design, and therefore the condition $c \ll r_0$ complies more weakly.

In the next section, such analysis is carried out to obtain an expression for the radiation resistance of the EC-SRR at its first resonance.

2.1.1 Radiation Resistance

As mentioned before, the SRR working around its first resonance is much smaller than the wavelength. It is also well known that the radiation properties of small particles are mainly determined by its first-order electric and magnetic moments (dipole moments). Hence, the first step in our analysis is to evaluate both moments, individually, on the basis of the current distribution of the EC-SRR.

Let us now focus on the magnetic dipole moment \mathbf{m}_A associated to the SRR external ring A. According the definition of dipole moment, this can be written as

$$\mathbf{m}_A = \frac{1}{2} \int_{V_A} \mathbf{r} \times \mathbf{J}_A dV_A, \quad (2.1)$$

where \mathbf{J}_A is the current density on the ring cross-section and V_A is the volume occupied by ring A. The exact evaluation of (2.1) requires the current density dependence over the r coordinate (i.e., over the ring width) to be known and expressed analytically. Due to the proximity effect [4] between the internal and external rings, the current is not uniformly distributed along the ring width (see Fig. 2.2), and at the first resonance it tends to accumulate far from the slot d because the currents in the rings flow in the same direction (Fig. 2.2a). The magnitude of the effect depends upon the position angle φ , and is minimized at $\varphi = 0$ and at $\varphi = \pi$ for the external and internal rings, respectively, due to the positions of the current zeroes and maxima on the SRR. That is, the current distribution is approximately uniform where the maxima i_0 occur, because the current on the other ring is zero. Since the zones around the current maxima provide the main contribution to the magnetic dipole moment, expression (2.1) can be evaluated to a good

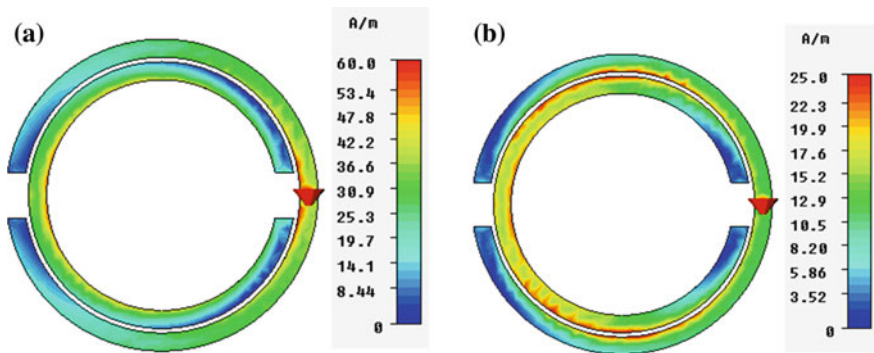


Fig. 2.2 Amplitude of the electric current density on the EC-SRR at the **a** first and **b** second resonance, simulated with CST Microwave Studio [$r_0 = 15$ mm ($\lambda_0/24$), $c = 2$ mm, $d = 0.5$ mm]. The input port is represented as a red triangle

approximation by assuming a uniform current distribution along the ring width at any position angle φ . Under this assumption, that is $\mathbf{J}_A = \mathbf{J}_A(z, \varphi, t)$, (2.1) leads to

$$\mathbf{m}_A = \frac{1}{2} \left(r_A^2 + \frac{c^2}{12} \right) \int_{-\pi}^{\pi} i_A(\varphi, t) d\varphi \hat{\mathbf{z}} \quad (2.2)$$

where c is the ring width and i_A is the current flowing on the external ring. Based on the quasi-static analysis, the current vector \mathbf{i}_A on the external ring at the angular frequency ω_0 can be expressed as

$$\mathbf{i}_A(\varphi, t) = i_0 \left(1 - \frac{|\varphi|}{\pi} \right) \cos(\omega_0 t) \hat{\boldsymbol{\varphi}}, \quad (2.3)$$

as represented in Fig. 2.1. Substitution of (2.3) into (2.2) and integration provide

$$\mathbf{m}_A = \frac{\pi}{2} \left(r_A^2 + \frac{c^2}{12} \right) i_0 \cos(\omega_0 t) \hat{\mathbf{z}}. \quad (2.4)$$

The magnetic dipole moment \mathbf{m}_B associated to the internal ring B can be evaluated by using the same method, and provides an expression analog to (2.4), with r_A changed for r_B . After some manipulation, the total magnetic dipole moment $\mathbf{m} = \mathbf{m}_A + \mathbf{m}_B$ can be written as

$$\mathbf{m} = \pi \left(r_0^2 + \frac{c^2}{3} + \frac{cd}{2} + \frac{d^2}{4} \right) i_0 \cos(\omega_0 t) \hat{\mathbf{z}}. \quad (2.5)$$

Expression (2.5) provides a good approximation to the problem. It shows that the magnetic dipole moment generated by the SRR at resonance is actually somewhat higher than that of a current loop of mean radius r_0 . However, even when the ring width c is increased up to $r_0/2$ (which could be taken as limit to ensure the correct operation of the resonator), all the terms depending from c and d in (2.5) can be neglected (note that d is usually maintained small in order to obtain reasonable coupling between the resonators). Therefore, for practical cases, (2.5) can always be reduced to

$$\mathbf{m} = \pi r_0^2 i_0 \cos(\omega_0 t) \hat{\mathbf{z}}, \quad (2.6)$$

which is the expression of the magnetic dipole moment associated to an infinitely thin current loop of amplitude i_0 and radius r_0 , and is the expression commonly used for the EC-SRR.

Let us now evaluate the resistance associated to the loop radiation. The power radiated by an electrically small magnetic moment of amplitude m_0 can be written as [5]:

$$P_{\text{rad}}^{\text{M}} = \frac{Z_0 k^4 m_0^2}{12\pi}, \quad (2.7)$$

where Z_0 is the free-space impedance and k is the free-space wavenumber. Therefore, by using (2.6), the radiation resistance associated to \mathbf{m} , referred to the current amplitude i_0 , can be found to be

$$R_{\text{rad}}^{\text{M}} = \frac{8}{3} \pi^5 Z_0 \left(\frac{r_0}{\lambda_0} \right)^4. \quad (2.8)$$

Since the size of the SRR mean radius in terms of wavelength is in the order of $1/20$, the radiation resistance associated to the axial magnetic dipolar moment \mathbf{m} is in the order of $1\text{--}2 \, \Omega$, though it strongly depends on the particle size (i.e., on the substrate thickness and permittivity, and on the magnitude of the coupling between rings).

As it is well known, the EC-SRR at its fundamental resonance also exhibits an electric dipole moment \mathbf{p} tangential to the plane of the particle, which arises from the bi-anisotropy of the structure. Such a dipole moment can be evaluated based on the electric charge distribution of the SRR, which can be inferred by applying the charge continuity law to the equation of the current profile (2.3) along the rings. Thus, the linear charge density λ_A on the external ring can be written as

$$\lambda_A(\varphi, t) = \frac{i_0}{\pi r_A \omega_0} \sin(\omega_0 t) \text{sgn}(\varphi). \quad (2.9)$$

Since expression (2.9) is odd with respect to the position angle φ (as a result of the electric wall along the xz -plane), the total electric dipole moment associated to ring A is the sum of the infinitesimal dipole moments directed along the $\hat{\mathbf{y}}$ direction, namely:

$$\mathbf{p}_A = \int_0^\pi \lambda_A(\varphi, t) 2r_A^2 \sin \varphi d\varphi \hat{\mathbf{y}}. \quad (2.10)$$

Once again, for simplicity, \mathbf{J}_A has been considered uniform through the ring width, so that the effective distance between charges is $2r_A \sin \varphi$. By integrating expression (2.10) we obtain

$$\mathbf{p}_A = \frac{4}{\pi} \frac{r_A}{\omega_0} i_0 \sin(\omega_0 t) \hat{\mathbf{y}}. \quad (2.11)$$

The internal ring B (with radius r_B) exhibits an electric dipole moment \mathbf{p}_B with the same orientation, but presents opposite sign, due to the ring cut position. Therefore, the total electric dipole moment \mathbf{p} is obtained by subtracting their amplitudes. By assuming the hypothesis of strong coupling between rings, which is normally satisfied at the first resonance, the current in the internal ring has roughly

the same amplitude i_0 as the current in the outer ring. Considering that $r_A - r_B = c + d$, the total electric dipole moment is

$$\mathbf{p} = \frac{4}{\pi\omega_0}(c+d)i_0 \sin(\omega_0 t)\hat{\mathbf{y}}. \quad (2.12)$$

Then, by using the Larmor equation [6] for the radiated power by a given electric dipole moment of amplitude p_0 , that is

$$P_{\text{rad}}^E = c_0^2 \frac{Z_0 k^4 p_0^2}{12\pi}, \quad (2.13)$$

where c_0 is the speed of light in vacuum, the radiation resistance associated to \mathbf{p} , and referred to the maximum current i_0 , can be expressed as follows:

$$R_{\text{rad}}^E = \frac{32}{3\pi} Z_0 \left(\frac{c+d}{\lambda_0} \right)^2. \quad (2.14)$$

Due to the proximity effect between rings, which was not taken into account in the analysis, the radiation resistance associated to the electric dipole moment is expected to be slightly higher than the value predicted by (2.14). This is because the effective distance between charges is actually higher than $c + d$, since the currents in the internal and external rings tend to separate each other.

Let us now compare (2.14) with (2.8). Since the typical values of $c + d$ in terms of wavelength are in the order of 1/100, that is, five or more times smaller than the mean radius r_0 , the radiation resistance associated to the electric dipole moment is in the order of 0.1 Ω , which is an order of magnitude smaller than the radiation resistance related to the magnetic dipole moment of the SRR. Therefore, the radiation resistance of the particle can be approximated by the resistance associated to the axial magnetic moment, that is

$$R_{\text{rad}} \approx R_{\text{rad}}^M. \quad (2.15)$$

2.1.2 Loss Resistance and Radiation Efficiency

As it is well known, the ohmic losses introduced by the metals in any structure strongly depend upon the current distribution \mathbf{J} inside the conductors. Hence, in order to provide an accurate estimation of the loss resistance, the skin effect and the proximity effect must be taken into account. Due to the skin effect, the current density distribution \mathbf{J} within the ring cross section decays exponentially from the surfaces, with a penetration depth (skin depth) depending on the working frequency f_0 and the metal conductivity σ (among others). Since the conductor thickness h is

usually much smaller than its width c , only the top and bottom faces are considered to carry current, neglecting the small contribution from the lateral faces.

The assumptions above lead to the following expression for \mathbf{J}_A (the current density in the outer ring) in phasorial form:

$$\mathbf{J}_A(r, \varphi, z) = \begin{cases} J_0(r)e^{-\gamma(z+\frac{h}{2})}\left(1 - \frac{|\varphi|}{\pi}\right)\hat{\boldsymbol{\phi}} & -\frac{h}{2} < z < 0 \\ J_0(r)e^{\gamma(z-\frac{h}{2})}\left(1 - \frac{|\varphi|}{\pi}\right)\hat{\boldsymbol{\phi}} & 0 < z < \frac{h}{2} \end{cases} \quad (2.16)$$

where $\gamma = (1 + j)/\delta$ is the complex propagation constant inside the conductor and δ is the skin depth, given by $\delta = (2/\omega\mu\sigma)^{1/2}$ [7], where μ and σ are the permeability and conductivity of the conductor material, respectively. The above expressions (for γ and δ) are valid for low-loss conductors, that is, for those satisfying $\sigma \gg \omega\epsilon$ (ϵ being the permittivity). As said in Sect. 2.1.1, the radial dependence of \mathbf{J}_A [i.e., $J_0(r)$] is cumbersome to be expressed analytically. However, an effective width $c_{\text{eff}} < c$ can be defined to account for the proximity effect, so that the current density is assumed to be uniform and equal to J_0 inside the effective width c_{eff} , and zero elsewhere. In the EC-SRR, the value of such effective section always depends on the width c (this is not true, for example, for the effective thickness h_{eff} associated to the skin effect, which does not depend on the thickness h when $h \gg \delta$) because there exist zones ($\varphi = 0$ and $\varphi = \pi$ for the external and the internal rings, respectively) of the rings where the current is distributed uniformly, and therefore all the cross-section is used. If the current is assumed to concentrate in an infinitely small area in the zones where the proximity effect is maximized (at $\varphi = \pi$ and $\varphi = 0$ for the external and the internal rings, respectively), and that a linear variation of the used section with the angle arises, the effective width can be approximated to $c_{\text{eff}} \approx \frac{1}{2}c$. As it will be shown at Sect. 2.2.2, this value works very well for the SRR at the second resonance, while a slightly higher value $c_{\text{eff}} = \frac{2}{3}c$ has been found to provide good results at the first resonance, and to agree with the expression proposed by Marques et al. in [8].

The power loss in the outer ring, inferred from the Ohm's law, is therefore

$$P_{\text{loss},A} = \frac{1}{2} \int_{-\pi}^{\pi} \int_{(-\frac{h}{2})}^{\frac{h}{2}} \int_{(r_A - \frac{c_{\text{eff}}}{2})}^{(r_A + \frac{c_{\text{eff}}}{2})} \frac{|\mathbf{J}_A(z, \varphi)|^2}{\sigma} r dr dz d\varphi \quad (2.17)$$

By solving (2.17) the power loss is found to be

$$P_{\text{loss},A} = \frac{\pi c_{\text{eff}} r_A \delta (1 - e^{-\frac{h}{\delta}})}{3\sigma} J_0^2. \quad (2.18)$$

The power loss in the inner ring can be obtained by using the same procedure. Thus, the total power loss can be written as

$$P_{\text{loss}} = \frac{2\pi c_{\text{eff}} r_0 \delta (1 - e^{-\frac{h}{\delta}})}{3\sigma} J_0^2. \quad (2.19)$$

Let us now compute the total current i_0 flowing at the input section ($\varphi = 0$), in order to calculate the loss resistance. By integrating the current density over the effective cross-sectional area, namely

$$i_0 = \int_{(-\frac{h}{2})}^{(\frac{h}{2})} \int_{(r_A - \frac{c_{\text{eff}}}{2})}^{(r_A + \frac{c_{\text{eff}}}{2})} (\mathbf{J}_A(0, z) \cdot \hat{\boldsymbol{\phi}}) dr dz, \quad (2.20)$$

the squared RMS (root mean square) current can be expressed as

$$\frac{|i_0|^2}{2} = J_0^2 c_{\text{eff}}^2 \delta^2 \left[1 + e^{-\frac{h}{\delta}} - 2e^{-\frac{h}{2\delta}} \cos\left(\frac{h}{2\delta}\right) \right]. \quad (2.21)$$

Finally, the loss resistance is obtained by dividing the power loss (2.19) by the squared RMS current (2.21), obtaining

$$R_{\text{loss}} = \frac{2\pi r_0}{3\sigma c_{\text{eff}} \delta} \left[\coth\left(\frac{h}{2\delta}\right) - \text{csch}\left(\frac{h}{2\delta}\right) \cos\left(\frac{h}{2\delta}\right) \right]^{-1}. \quad (2.22)$$

The hyperbolic function on the right side of (2.22) can be approximated by the hyperbolic cotangent with the same argument, that is

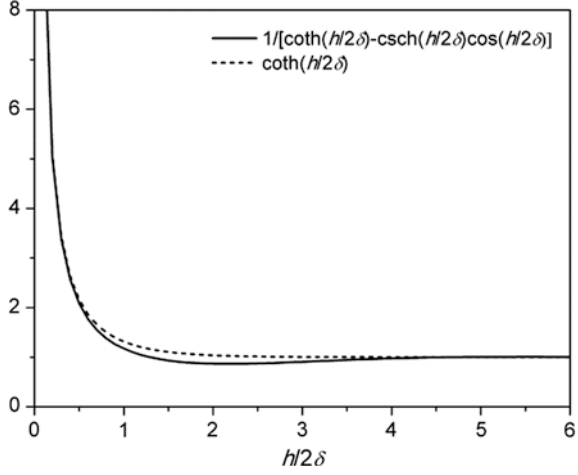
$$\left[\coth\left(\frac{h}{2\delta}\right) - \text{csch}\left(\frac{h}{2\delta}\right) \cos\left(\frac{h}{2\delta}\right) \right]^{-1} \approx \coth\left(\frac{h}{2\delta}\right) \quad (2.23)$$

with a maximum error of 20% for $h = 3.7 \delta$ (see Fig. 2.3). We will later show that, for practical cases, the error introduced by approximation (2.23) is reduced to a few percentage points in the expression of the radiation efficiency, so that (2.23) provides a substantial simplification of the formulas while maintaining good accuracy in the results. In fact, by combining (2.22) and (2.23), the loss resistance can be expressed in a very simple form, that is

$$R_{\text{loss}} \approx \frac{2\pi r_0}{3\sigma c_{\text{eff}} \delta} \coth\left(\frac{h}{2\delta}\right). \quad (2.24)$$

As said above, the value of effective width providing good agreement with the simulated results is $c_{\text{eff}} = 2/3 c$. Therefore, the final expression for the loss resistance of the SRR around its fundamental resonance is found to be

Fig. 2.3 Comparison between the functions in the left (solid line) and right (dashed line) hand of Eq. (2.23)



$$R_{\text{loss}} \approx \frac{\pi r_0}{\sigma c \delta} \coth\left(\frac{h}{2\delta}\right). \quad (2.25)$$

It is worth mentioning that (2.25) converges to the values provided in [8] when the metal thickness approaches the values $h \ll 2\delta$ and $h \gg 2\delta$, and additionally describes the behavior of the loss resistance for intermediate values of h .

Let us now discuss the radiation efficiency at resonance, η_{rad} . To this end, it is worth mentioning that the equivalent circuit model of the SRR at resonance, usually being reported to be a shunt LC circuit [3], becomes a series RLC circuit when the particle is excited through a cut opened in one ring, and both radiation and losses are considered (a simulated and experimental validation of this fact will be provided in Sect. 3.1.1). Therefore, the ohmic losses in the SRR can be modeled by a resistance placed in series with the radiation resistance, so that the radiation efficiency (neglecting dielectric losses) is also the ratio between the radiation resistance R_{rad} and the total resistance $R_{\text{rad}} + R_{\text{loss}}$. Based on this consideration, and on the previous analysis, it follows that

$$\eta_{\text{rad}} \approx \left[1 + \frac{3}{8} \frac{c_0^4 \sqrt{\pi \mu_0}}{\pi^4 Z_0} \left(c r_0^3 \sqrt{f_0^7 \sigma} \right)^{-1} \coth\left(\frac{h}{2\delta}\right) \right]^{-1}, \quad (2.26)$$

where μ_0 is the permeability of free-space and f_0 is the working frequency. Expression (2.26) does not take into account dielectric losses, which strongly depend on the dielectric properties and the thickness of the substrate, and require integration of the fields over the substrate volume to be calculated.

In order to validate (2.26), and consequently, the expressions obtained above for the radiation (see previous section) and loss resistance, full-wave simulations of an EC-SRR without dielectric substrate were carried out by means of the commercial

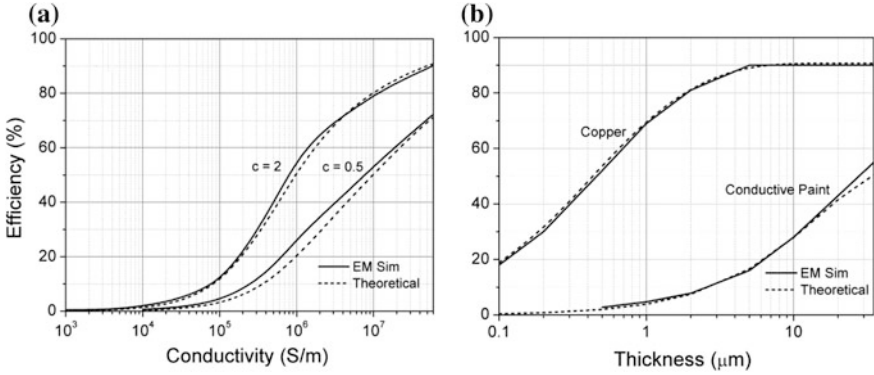


Fig. 2.4 Theoretical and simulated results for the radiation efficiency of the EC-SRR at the first resonance, as a function (a) of the metal conductivity (for different values of trace width c , with metal thickness $h = 35 \mu\text{m}$) and (b) thickness (for trace width $c = 2 \text{ mm}$). The conductivity of the conductive paint is set to 10^6 S/m [25, 26]

software *ADS Momentum*. The simulated structure was fed by a differential port placed across a cut (0.2 mm) opened in the external ring at the position $\varphi = 0$, and the dimensions of the SRR were adjusted to locate the resonance at $f_0 = 1 \text{ GHz}$, obtaining $r_0 = 15 \text{ mm}$ ($\lambda_0/20$) and $d = 0.5 \text{ mm}$. In the first set of simulations, the efficiency was found as a function of the metal conductivity σ for two different values of c (Fig. 2.4a), setting the metal thickness to $h = 35 \mu\text{m}$. In the second set, the width was fixed to $c = 2 \text{ mm}$, and the efficiency was depicted as a function of the metal thickness h for different materials (Fig. 2.4b). In both cases, good agreement between (2.26) and EM simulation was obtained. As can be seen in Fig. 2.4a, the antenna efficiency strongly depends on the ring width c , which is therefore one of the most important design parameters of the SRR antenna.

2.1.3 Far-Field Radiation Pattern and Quality Factor

According to the analysis of the previous section, the main radiation mechanism of the EC-SRR at the first resonance is attributed to the electrically small current loop which results from the current distribution in the external and internal rings. Hence, in a first approximation, the SRR is expected to produce a linearly polarized omni-directional radiation, with maximum power density in the xy -plane (E -plane) and a theoretical directivity of 1.5 (1.76 dBi) [9]. However, the presence of the electric dipole moment introduces some changes in the fields radiated by the resonator. First, it generates a cross-polarization component. In fact, if the radiation produced by the magnetic dipole moment is defined as co-polar (being the main radiation mechanism), the contribution from the electric dipole moment is entirely cross-polar in the yz -plane ($\varphi = \pi/2$), due to the orthogonality and the 90° phase

shift [see (2.6) and (2.12)] between the two radiators. Note that, in the xz -plane, the electric dipole radiation does not contribute to the formation of cross-polarization components, because the fields radiated by the loop and the dipole are oriented towards the same direction ($\hat{\phi}$ for the electric field). It is useful to define the quantity

$$XPOL_{\max} = \frac{R_{\text{rad}}^E}{R_{\text{rad}}^M} = \frac{4}{\pi^6} \left(\frac{c+d}{\lambda_0} \right)^2 \left(\frac{r_0}{\lambda_0} \right)^{-4}, \quad (2.27)$$

which represents the maximum value of the cross-polar component (which occurs at $\theta = 0$), normalized to the maximum value of the co-polar (which occurs at $\theta = \pi/2$) in the yz -plane. This can be deduced by assuming that the radiation patterns of the magnetic and electric moments present the same shape (i.e., both are elemental radiators). The value of $XPOL_{\max}$ controls several characteristics of the far-field, in terms of gain and axial ratio (defined as the ratio between the major and minor axis of the ellipse described by the electric field of the radiated plane wave). In the yz -plane, the gain in the axial (z -axis) direction is found analytically to be $XPOL_{\max}$ times the gain in the endfire direction (y -axis). Furthermore, four zones where the axial ratio decays down to unity exist in the yz -plane. In fact, since the co-polar radiation is proportional to $\sin^2(\theta)$ and the cross-polar is proportional to $\cos^2(\theta)$, circular polarization is generated at the four angles

$$\theta_c = \{\pm tg^{-1}(\sqrt{XPOL_{\max}}), \pm tg^{-1}(\sqrt{XPOL_{\max}}) + \pi\}, \quad (2.28)$$

and the axial ratio maintains under an arbitrary level AR_0 (e.g., $AR_0 = 10$ dB can be considered for linear polarization) in each of the four regions centered in θ_c and subtending an angle equal to

$$\Delta\theta_{\text{ell}} = tg^{-1}(AR_0\sqrt{XPOL_{\max}}) - tg^{-1}(AR_0^{-1}\sqrt{XPOL_{\max}}), \quad (2.29)$$

where elliptical polarization is produced. It was verified by simulation that, for values of AR_0 in the order of 10 dB, each of these regions describes approximately a cone in the radiating sphere, thus enclosing a solid angle $\Omega_{\text{ell}} \approx 2\pi[1 - \cos(\Delta\theta_{\text{ell}}/2)]$. This expression can be used to quantify the polarization purity across the radiating space of tags based on the SRR antenna, as in the case of the design presented in the next chapter.

In terms of radiation diagram, the presence of the electric dipole radiation distorts the omni-directional pattern of the current loop in the xy -plane to a bi-directional pattern, with maxima at $\varphi = \{0, \pi\}$. As reported in [10], this kind of pattern results from the 90° phase-shift between an electric and a magnetic radiator oriented orthogonally. It is interesting to relate the minimum antenna gain G_z , which occurs in the axial direction (or $\theta = 0$) to the maximum antenna gain G_x , occurring in the xy -plane at $\varphi = \{0, \pi\}$. It was found that

$$\frac{G_z}{G_x} \approx \frac{XPOL_{\max}}{1 + XPOL_{\max}}. \quad (2.30)$$

Expression (2.30) assumes that the magnetic dipole moment produces a perfectly omni-directional pattern in the xy -plane. However, since the sum of the inner and outer currents in the SRR is only approximately a constant function of φ , the assumption made above is not strictly satisfied, so that expression (2.30) should be considered as an approximation. In the next chapter, the formula will be used in order to relate the minimum read range to the maximum read range of UHF-RFID tags based on the SRR antenna at its first resonance, and an experimental validation will be provided.

As it is expressed in (2.27), the value of $XPOL_{\max}$ is controlled by the SRR mean radius and the distance $c + d$ (which is also the radius difference $r_A - r_B$). For very small values of $c + d$, the cross-polarization level can be lowered to -20 dB/ -25 dB (according to simulation results). However, this involves a reduction of the radiation efficiency, as predicted by (2.26), so that the typical values of $XPOL_{\max}$ at the first resonance for efficient EC-SRR antenna designs are in the range of -8 dB/ -10 dB. In any case, the value of $XPOL_{\max}$ is much smaller than unity, because the distance $c + d$ cannot be increased indefinitely. As a result, the solid angle Ω_{ell} is much smaller than 4π (which represents the solid angle of the sphere) in any case, and therefore the EC-SRR radiation can be considered linearly polarized on most of the radiating sphere.

The radiation pattern described above, along with the cross-polarization level predicted in (2.27), was validated by the far-field EM simulations (experimental validation of the SRR antenna radiation pattern will be provided at Sect. 3.1). To this end, two different lossless EC-SRR layouts with very different values of $c + d$ (2.5 and 0.7 mm) were simulated, and the far-field characteristics were compared. The results, in terms of radiation diagram and axial ratio, are depicted in Fig. 2.5. As expected, the radiation of the SRR can be modeled by the sum of an axial magnetic moment (main radiator) and an electric moment oriented towards the y -axis (secondary radiator). Moreover, the levels of the cross-polar radiation rise when the value of $c + d$ is increased, and the elliptical region gradually narrows and orientates toward the radiation minima, as predicted by theory. However, the simulated values of $XPOL_{\max}$ are higher than the predicted values (see Table 2.1 for a comparison). We attribute this disagreement to the second order effects (e.g., the proximity effect, which is expected to increment the electric dipole moment) which were not taken into account in the analysis. Hence, (2.27) should be taken as a first approximation which allows easily understanding the behavior of the EC-SRR cross-polarization as a function of its geometrical parameters. The simulated antenna directivity is $D_0 = 1.6$ dBi for $c + d = 2.5$ mm and $D_0 = 2$ dBi for $c + d = 0.7$ mm; both values are similar to the directivity of an elemental radiator (1.76 dBi).

Let us now discuss the EC-SRR antenna quality factor at the first resonance, which determines the maximum bandwidth that can be obtained with conjugate

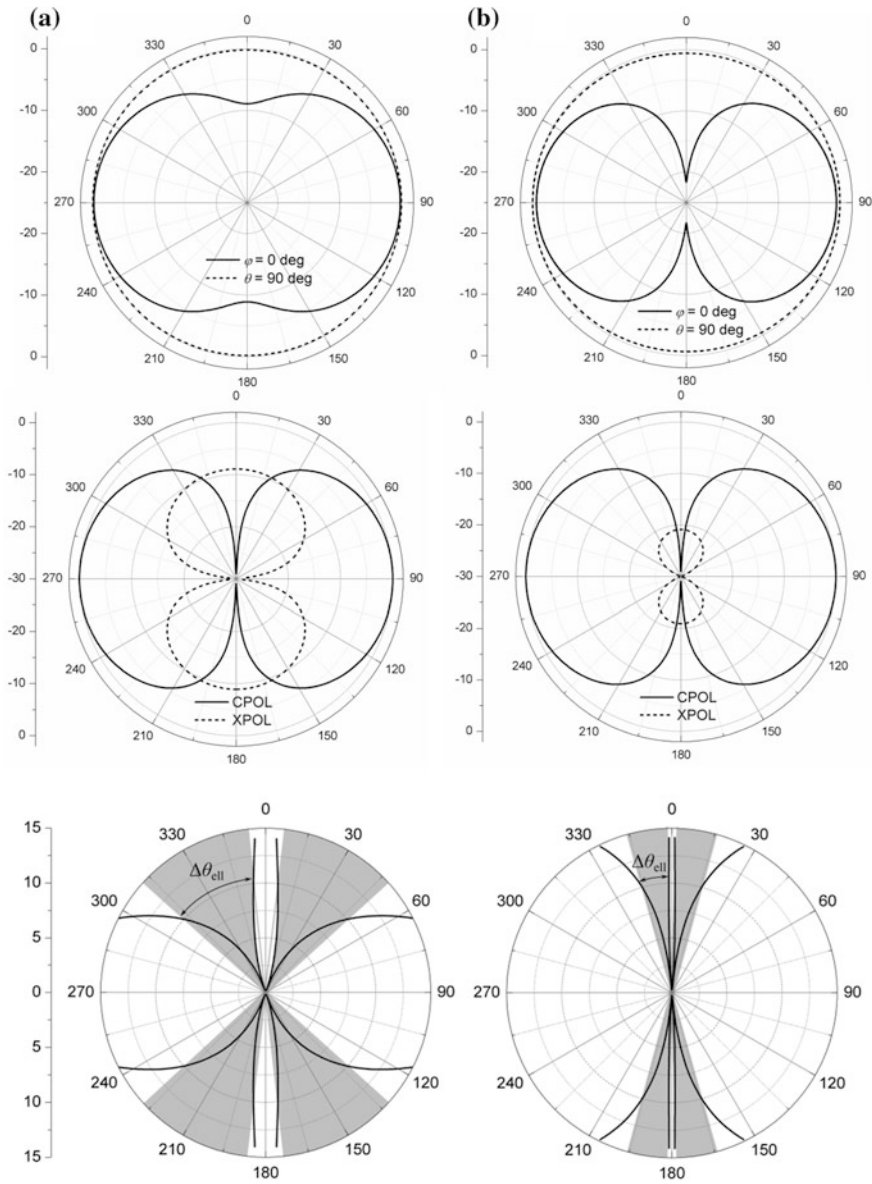


Fig. 2.5 Top Simulated normalized radiation pattern at $\phi = 0^\circ$ (xz -plane) and $\theta = 90^\circ$ (xy -plane), middle co-polar and cross-polar components in the yz -plane and bottom axial ratio in the yz -plane, of a lossless EC-SRR at the first resonance for **a** $c + d = 2.5$ mm and **b** $c + d = 0.7$ mm. The value of r_0 is 15 mm. The low axial ratio (≤ 10 dB) region is depicted in grey

Table 2.1 Theoretical and simulated values of $XPOL_{\max}$ for the EC-SRR at the first resonance

	Theoretical (dB)	EM simulation (dB)
$c + d = 2.5$ mm	-13	-9
$c + d = 0.7$ mm	-25	-21

impedance matching. Due to the physical limitations affecting small planar antennas, discussed at Sect. 1.4.2, the quality factor and bandwidth are limited to the values provided by Eqs. (1.2) and (1.3), respectively. Considering that, at the first resonance, the mean radius (and consequently the external radius) is in the order of $1/20$ times the free-space wavelength and assuming that the radiation efficiency approaches unity, the half-power fractional bandwidth is expected to be $FBW \leq 1\text{--}2\%$, corresponding to roughly 10–20 MHz at the UHF-RFID band. While this value could be considered poor for some communication applications, it is suitable for UHF-RFID tags, where the required bandwidth is limited to few megahertz.

The abovementioned equations set the lower bound for the quality factor of any small antenna confined to a planar geometry. In practice, the SRR antenna is expected to provide a higher quality factor, which can be predicted on the basis of its equivalent circuit model near the resonance, i.e., a series RLC resonator, which provides $Q_{\text{rad}} = \omega_0 L / R_{\text{rad}}$. The value of the EC-SRR self-inductance L can be computed as the average of the inductances of both rings [3], that is the inductance of a loop with radius r_0 and width c . A commonly used approximation for the inductance of a circular loop is $L \approx \mu_0 r_0 [\ln(16r_0/c) - 2]$, which assumes a circular section with radius $c/2$. Hence, by using (2.15) for the radiation resistance, the half-power fractional bandwidth of the SRR antenna, in the case of conjugate matching, can be approximated to

$$FBW \approx \frac{8}{3} \pi^4 \eta_{\text{rad}}^{-1} \left[\ln \left(16 \frac{r_0}{c} \right) - 2 \right]^{-1} \left(\frac{r_0}{\lambda_0} \right)^3. \quad (2.31)$$

Expression (2.31) assumes that the input resistance of the port driving the antenna does not vary in frequency. This condition is not strictly satisfied in the case of RFID ASICs, which are modeled by shunt RC circuits. However, the variation of the ASICs input resistance R_C is usually very small within the UHF-RFID band [11], so that (2.31) can be used for the tag bandwidth to a good degree of approximation. For practical cases, the values found by using (2.31) are in the order of $FBW \approx 0.8 - 1\%$, when radiation efficiency near unity is obtained. Although this value does not allow a worldwide operation of the tag, it is large enough for ensuring its correct operation in one of the UHF-RFID bands. It is worth to mention that ohmic and dielectric losses decrease the overall quality factor, thus increasing the bandwidth at the expense of a reduction of the tag peak read range. Equation (2.31) will be verified by means of EM simulation and measurements at

Sect. 3.1.1, where an UHF-RFID tag based in the EC-SRR antenna will be presented.

2.2 EC-SRR at Its Second Resonance

In this section, the study of the EC-SRR radiation resistance will be extended to the case of working around the second resonance of the structure, where the currents in the external and internal rings flow in opposite directions [12]. Due to the increased particle dimensions and the different current distribution, the quasi-static analysis presented at the previous section does not hold for the second resonance. However, the EC-SRR dimensions at its second resonance are still very near to the commonly accepted boundary of electrically small antennas ($ka = 0.5$), since its radius is typically in the order of 0.1 free-space wavelength, corresponding to $ka \approx 0.6$. Therefore, its radiation properties can still be predicted to a good degree of approximation by evaluating the first order (dipole) terms of the electric and magnetic moments generated by the current distribution, and treat such sources as elemental radiators.

2.2.1 Radiation Resistance

At the second resonance, the currents in the outer and inner rings flow in opposite directions [12], and the current distribution approximately satisfies $i_A(\varphi) = -i_B(\varphi \pm \pi)$, where i_A and i_B is the current in the external (A) and internal (B) ring, respectively, and φ is the angular position with respect to the x -axis. This relation is valid if the distance between rings, d , is small as compared to the mean ring radius r_0 (strong coupling condition). Since the length of each ring is approximately half-wavelength, the current along the ring circumference can be assumed to exhibit a sinusoidal profile (Fig. 2.6), with a maximum value at the center ($\varphi = 0$ for ring A and $\varphi = \pm\pi$ for ring B), and null at the ring edges (approximated to $\varphi = \pm\pi$ for ring A and $\varphi = 0$ for ring B). However, as it is corroborated later (see Fig. 2.7b), the current in each ring actually exhibits a slight discrepancy to this approximation, mainly because the length of each ring at the second SRR resonance is somewhat greater than the half-wavelength at the working frequency. Nevertheless, by means of this sinusoidal approximation to the rings currents, analytical expressions can be found, and good agreement between theory, simulation and experiment is obtained. Moreover, as in the previous section, the proximity effect will not be taken into account in the calculation of the radiation resistance, in order to maintain the expressions simple and to show that such effect does not substantially affect the result.

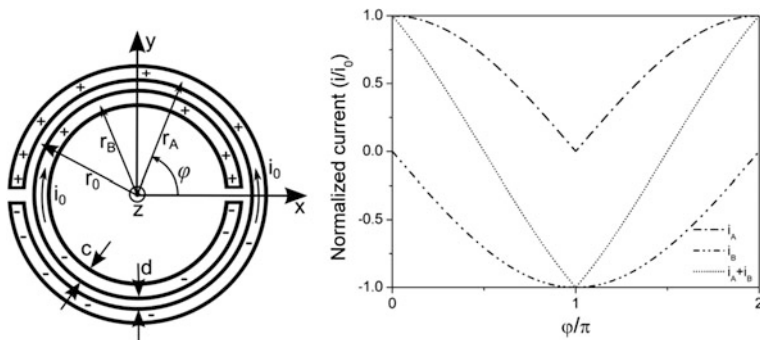


Fig. 2.6 Topology and theoretical electric current/charge distribution of the EC-SRR at its second resonance. *Left image* reprinted with permission from [27]

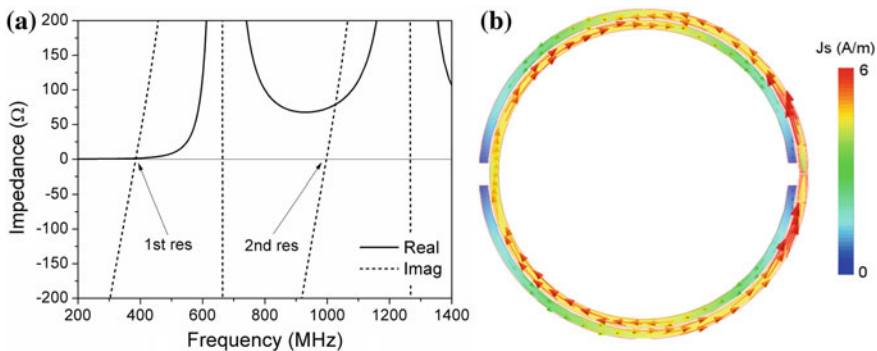


Fig. 2.7 Simulated **a** input impedance and **b** electric current distribution at the second resonant frequency (1 GHz) of a lossless EC-SRR (no dielectric substrate is considered). *Left image* reprinted with permission from [27]

The current in the external ring, of mean radius r_A , can thus be written as:

$$i_A(\varphi, t) = i_0 \cos\left(\frac{\varphi}{2}\right) \cos(\omega_0 t) \hat{\varphi}. \quad (2.32)$$

By solving the well-known electric charge continuity equation, the linear charge density in the ring is found to be

$$\lambda_A(\varphi, t) = \frac{i_0 \sin\left(\frac{\varphi}{2}\right) \sin(\omega_0 t)}{2r_A \omega_0}. \quad (2.33)$$

As in the case of the analysis at the first resonance, expression (2.10) can be used to evaluate the electric dipole moment associated to the external ring, obtaining

$$\mathbf{p}_A = \frac{4}{3} \frac{r_A}{\omega_0} i_0 \sin(\omega_0 t) \hat{\mathbf{y}}. \quad (2.34)$$

The internal ring B , of mean radius r_B , exhibits an electric dipole moment with the same orientation and phase, so that the total dipole moment amplitude is the sum of the internal and external dipole moments amplitudes, leading to

$$\mathbf{p} = \frac{8}{3} \frac{r_0}{\omega_0} i_0 \sin(\omega_0 t) \hat{\mathbf{y}}. \quad (2.35)$$

Since the radiating particle is electrically small, it is still possible to consider the total moment given by (2.35) as an infinitesimal electric dipole moment located in the y -axis. Thus, by using the Larmor equation [6] for the radiated power by a given electric dipole moment of amplitude p_0 , the total radiation resistance referred to the maximum current i_0 can be expressed as

$$R_{\text{rad}}^E = \frac{128}{27} \pi Z_0 \left(\frac{r_0}{\lambda_0} \right)^2 \approx 5600 \left(\frac{r_0}{\lambda_0} \right)^2 \Omega. \quad (2.36)$$

It is interesting to compare the value found in (2.36) with the radiation resistance of a small dipole, which can be expressed by means of the well-known expression:

$$R_{\text{rad}0} = 20\pi^2 \left(\frac{l}{\lambda_0} \right)^2 \approx 790 \left(\frac{r}{\lambda_0} \right)^2 \Omega \quad (2.37)$$

where r is the length of each dipole arm. As can be seen by comparing (2.36) and (2.37), for a given radiator size (r_0 for the SRR or r for the dipole), the SRR working at the second resonance exhibits a much higher radiation resistance as compared to a small electric dipole. This can be explained arguing that the SRR takes advantage of most of the area enclosed by its lateral dimensions, while the dipole only distributes its charges along a line.

Let us now compute the magnetic dipole moment associated to EC-SRR at the second resonance. By solving (2.1), the magnetic contribution associated to the external ring is found to be

$$\mathbf{m}_A = 2r_A^2 i_0 \cos(\omega_0 t) \hat{\mathbf{z}}. \quad (2.38)$$

As explained above, the current in the internal ring flows in the opposite direction, and generates an opposite axial magnetic dipole moment. Therefore, the total magnetic dipole moment can be written as:

$$\mathbf{m} = 4r_0(r_A - r_B) i_0 \cos(\omega_0 t) \hat{\mathbf{z}}. \quad (2.39)$$

As in the previous case (Sect. 2.1.1), the radiation resistance associated to the magnetic dipole moment, referred to the current maximum i_0 , can be found by using (2.7). Taking into account that $r_A - r_B = c + d$, it is found that

$$R_{\text{rad}}^{\text{M}} = \frac{128}{3} \pi^3 Z_0 \left(\frac{r_0}{\lambda_0} \right)^2 \left(\frac{c+d}{\lambda_0} \right)^2. \quad (2.40)$$

It can be easily verified that, due to a nearly complete cancellation of the axial magnetic moments of the internal and external rings, the power radiated by the magnetic dipole at the second resonance is much smaller (two orders of magnitude) than the power associated to the electric dipole. Therefore, to a good approximation, the radiation resistance of the particle is dominated by the one associated to its electric dipole moment, that is,

$$R_{\text{rad}} \approx R_{\text{rad}}^{\text{E}}. \quad (2.41)$$

The potential of SRRs as radiating elements operating at their second resonance is demonstrated by evaluating (2.41) for typical values of r_0/λ_0 , which are in the order of 0.1. The resulting radiation resistance values are very close to the radiation resistance of the commonly used, and very well-known, half-wave dipole antenna (73 Ω). This fact suggests that half-wave dipole antennas can be replaced with SRRs (operating at the second resonance) without the need of a matching network, thereby reducing the maximum dimension of the antenna (defined as the radius of the minimum sphere enclosing the antenna) by a factor 2.5, approximately.

In order to validate the analysis presented above, an EC-SRR was simulated by means of the commercial software *Agilent Advanced Design System (ADS)*. The geometry of the particle was adjusted to locate the second resonance at the frequency $f_0 = 1$ GHz ($\lambda_0 = 300$ mm) when no substrate is used. The values for the geometric parameters are $r_0 = 35.25$ mm ($\lambda_0/8.5$), $c = 2$ mm, $d = 0.5$ mm, and the cut width was set to 5 mm.

The discrete port was placed across a 0.4 mm gap opened at the center of the external ring ($\varphi = 0^\circ$), where a current maximum i_0 is expected to occur. Therefore, in a lossless case, the input resistance R_{in} of the system corresponds to the radiation resistance R_{rad} of the particle. Hence, in the first set of simulations the metal is treated as a perfect conductor, in order to isolate the radiation resistance of the SRR and to verify (2.41).

The simulated input impedance of the SRR (without dielectric substrate), depicted in Fig. 2.7a, clearly reveals the first (0.4 GHz) and second (1 GHz) resonant frequencies of the SRR, and the first anti-resonant frequency (0.66 GHz), which corresponds to the intrinsic resonance of the inner ring. Note also that the radiation resistance at the second resonance (73 Ω) is nearly two orders of magnitude greater than the radiation resistance at the first resonance (1 Ω), and is exactly equal to the radiation resistance of a canonical half-wave dipole. The simulated electric current density distribution at the second resonance (Fig. 2.7b) is in good agreement with the approximated theoretical distribution described at the

beginning of this section, i.e., the current in the internal and external rings flow in opposite directions, and their amplitudes are similar. However, since the length of each ring is slightly greater than half-wavelength, the maximum at the center of the rings splits into two maxima symmetrically positioned around the center. Nevertheless, expression (2.32) is a useful approximation, as it allows simplifying the analytical treatment maintaining high accuracy in the results.

In order to validate (2.41), a lossless dielectric of thickness $h_s = 2.54$ mm was then added as substrate, allowing to control the value of the second resonance frequency f_0 , and consequently the value of λ_0 . By increasing the dielectric permittivity ϵ_r of the substrate, the value of r_0/λ_0 was gradually decreased, and the simulated input resistance of the particle was compared in each case to the radiation resistance calculated by (2.41). The results, depicted in Fig. 2.8, reveal that there is very good agreement between theory and simulation.

It is worth to mention that, to modulate the electrical size of the particle without changing the substrate dielectric constant, it is also possible to vary the coupling between rings, mainly controlled by the slot width d . In fact, according to the theory of coupled resonators [13], decreasing the coupling (while fixing r_0) reduces the frequency split between first and second resonance. Therefore, the second resonance is lowered and the particle becomes electrically smaller, providing an additional degree of freedom at the design stage. However, only relatively small changes of r_0/λ_0 are possible by using this technique. Moreover, if the coupling between rings is very small, the assumptions for the derivation of Eqs. (2.35) and (2.39) no longer hold. The reason is that the difference between the internal and external rings radii increases with the distance d , and the internal and external current amplitudes diverge as well.

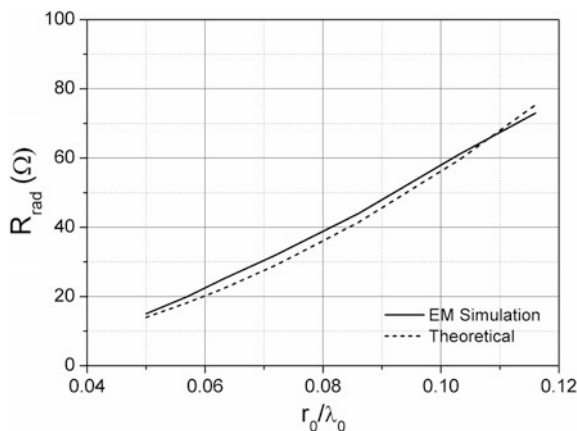


Fig. 2.8 Radiation resistance at the second resonance as a function of the EC-SRR mean radius relative to the wavelength. Note that the radiation resistance is roughly 73 Ω (i.e., the radiation resistance value of a half-wave dipole) for $r_0/\lambda_0 = 0.118$. Reprinted with permission from [27]

2.2.2 Loss Resistance and Radiation Efficiency

The assumptions regarding the current density distribution along the EC-SRR cross-section (Sect. 2.1.2) still hold at the second resonance. In this case, however, the current dependency over the position angle φ is different, being imposed by (2.32). Therefore, the following expression for \mathbf{J}_A (the current density in the outer ring) in phasorial form can be written as

$$\mathbf{J}_A(r, \varphi, z) = \begin{cases} J_0(r)e^{-\gamma(z+\frac{h}{2})} \cos(\frac{\varphi}{2}) \hat{\boldsymbol{\phi}} & -\frac{h}{2} < z < 0 \\ J_0(r)e^{\gamma(z-\frac{h}{2})} \cos(\frac{\varphi}{2}) \hat{\boldsymbol{\phi}} & 0 < z < \frac{h}{2} \end{cases} \quad (2.42)$$

As reported in Sect. 2.1.2, an effective width $c_{\text{eff}} < c$ can be defined to account for the proximity effect, so that the current density $J_0(r)$ is taken to be uniform and equal to J_0 inside the effective width c_{eff} , and zero elsewhere. If the current is assumed to concentrate in an infinitely small area in the zones where the proximity effect is maximized ($\varphi = \pi$ and $\varphi = 0$ for the external and the internal rings, respectively), and that a linear variation of the used section with the angle arises, the effective width can be approximated to $c_{\text{eff}} \approx c/2$.

The power loss on the outer ring can be calculated by using (2.17), leading to

$$P_{\text{loss,A}} = \frac{\pi c_{\text{eff}} r_A \delta (1 - e^{-\frac{h}{\delta}})}{2\sigma} J_0^2, \quad (2.43)$$

so that the total power loss is found to be

$$P_{\text{loss}} = \frac{\pi c_{\text{eff}} r_0 \delta (1 - e^{-\frac{h}{\delta}})}{\sigma} J_0^2. \quad (2.44)$$

Starting from (2.44), the procedure described at Sect. 2.1.2 [involving expressions (2.21) and (2.23)] can be used to evaluate the loss resistance, obtaining

$$R_{\text{loss}} \approx \frac{\pi r_0}{\sigma c_{\text{eff}} \delta} \coth\left(\frac{h}{2\delta}\right). \quad (2.45)$$

As mentioned above, the effective width can be approximated by $c_{\text{eff}} \approx c/2$, leading to the final expression for the loss resistance of the EC-SRR at the second resonance:

$$R_{\text{loss}} \approx \frac{2\pi r_0}{\sigma c \delta} \coth\left(\frac{h}{2\delta}\right). \quad (2.46)$$

Let us now discuss the radiation efficiency of the EC-SRR at the second resonance. As it was found in the previous section, the ohmic losses can be modeled by

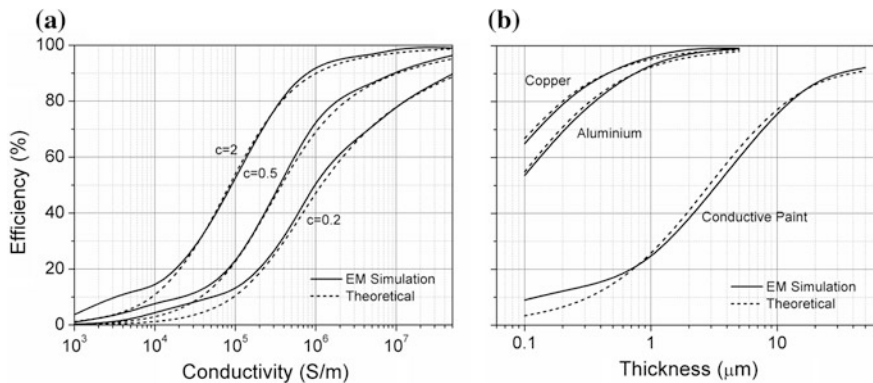


Fig. 2.9 Simulated and theoretical radiation efficiency of the EC-SRR at the second resonance, **a** versus conductivity for $h = 35 \mu\text{m}$ and **b** versus conductor thickness for $c = 2 \text{ mm}$. The considered conductive paint has a conductivity $\sigma = 10^6 \text{ S/m}$ [25, 26]. Reprinted with permission from [27]

a resistance placed in series with the radiation resistance. Therefore, the radiation efficiency η_{rad} can be expressed as

$$\eta_{\text{rad}} \approx \left[1 + \frac{27}{64} c_0 \sqrt{\frac{\pi}{\mu_0}} \left(c r_0 \sqrt{f_0^3 \sigma} \right)^{-1} \coth \left(\frac{h}{2\delta} \right) \right]^{-1}. \quad (2.47)$$

The expression above was validated by EM simulation. To this end, ohmic losses were added to the metal layer of the simulated structure presented in the previous section [$f_0 = 1 \text{ GHz}$ without dielectric substrate, $r_A = 36.5 \text{ mm}$, $r_B = 34 \text{ mm}$ $c = 2 \text{ mm}$, $d = 0.5 \text{ mm}$, $r_0 = 35.25 \text{ mm}$ ($\lambda_0/8.5$), cut width 5 mm]. The simulated radiation efficiency as a function of the metal conductivity for different values of the strip width c , setting the value of the metal thickness to $h = 35 \mu\text{m}$, is shown in Fig. 2.9a. The thickness dependence of the radiation efficiency for a strip width of $c = 2 \text{ mm}$ is simulated and depicted in Fig. 2.9b for different materials. Very good agreement between electromagnetic simulations and theoretical predictions is observed for efficiency values greater than 15%, which is the region of interest in practical antennas.

2.2.3 Far-Field Radiation Pattern and Quality Factor

Since the main radiation mechanism of the EC-SRR at the second resonance is the tangential electric dipole moment oriented along the y -axis (see Fig. 2.6), the structure is expected to produce a linearly polarized omni-directional radiation, with maximum power density at $\theta = \{0, \pi\}$ and a theoretical directivity of 1.5 (1.76 dBi).

However, due to the non-zero length of the particle in the x direction (the structure can be seen as an array of near elements radiating in phase), a slightly bi-directional pattern is expected over the xz -plane ($\varphi = 0$), thus resulting in a higher value of the directivity. Moreover, the presence of a magnetic dipole moment oriented along the z -axis generates radiation, which is entirely cross-polar in the yz -plane (E -plane), as in the case of the electric dipole radiation at the first resonance (Sect. 2.1.3). In this case, the cross-polar radiation is maximized at $\theta = \pi/2$. Hence, in this direction the value of the cross-polarization level is maximized, and it can be evaluated by dividing (2.40) by (2.36), obtaining:

$$XPOL_{\max} = 9\pi^2 \left(\frac{c+d}{\lambda_0} \right)^2. \quad (2.48)$$

Notice that, unlike in the case of the first resonance [see Eq. (2.27)], the value of $XPOL_{\max}$ does not depend on the SRR mean radius.

The considerations made in the previous section, about the effect of $XPOL_{\max}$ over the radiation pattern and the axial ratio, still hold at the second resonance. However, in this case the low axial ratio zones are centered on the angles

$$\theta_c = \left\{ \pm tg^{-1}(\sqrt{XPOL_{\max}^{-1}}), \pm tg^{-1}(\sqrt{XPOL_{\max}^{-1}}) + \pi \right\}, \quad (2.49)$$

and the region with elliptical polarization is comprised in

$$\Delta\theta_{\text{ell}} = tg^{-1}(AR_0\sqrt{XPOL_{\max}^{-1}}) - tg^{-1}(AR_0^{-1}\sqrt{XPOL_{\max}^{-1}}). \quad (2.50)$$

The simulated results for the radiation pattern and the axial ratio of a lossless EC-SRR at the second resonance are depicted in Fig. 2.10 [$f_0 = 1$ GHz, $r_A = 36.5$ mm, $r_B = 34$ mm, $c = 2$ mm, $d = 0.5$ mm, $r_0 = 35.25$ mm ($0.118 \lambda_0$), cut width 5 mm]. The normalized radiation pattern in the yz -plane confirms that the main radiation mechanism is the electric dipole oriented along the y -axis, and the value of the cross-polarization level is $XPOL_{\max} = -22$ dB, in perfect agreement with the theoretical value predicted by (2.48). As expected, such a small value of the cross-polarization level provides a very small elliptical radiation area ($\Delta\theta_{\text{ell}} = 10^\circ$), centered very near to the radiation minima, so that the radiation provided by the magnetic moment does not practically affect the polarization of the radiated fields. Regarding the xz -plane ($\varphi = 0$), the pattern is slightly bi-directional, due to the array effect associated to the non-zero length of the particle in the x -direction (notice that, at the first resonance, the lateral dimensions of the particle in terms of wavelengths are sensibly smaller, and therefore a quasi-circular pattern is obtained). As a result, the directivity is increased, and reaches $D_0 = 2.7$ dBi according to the simulations.

Let us now treat the quality factor of the EC-SRR at the second resonance. Due to the greater dimensions of the particle in terms of wavelength, the quality factor of

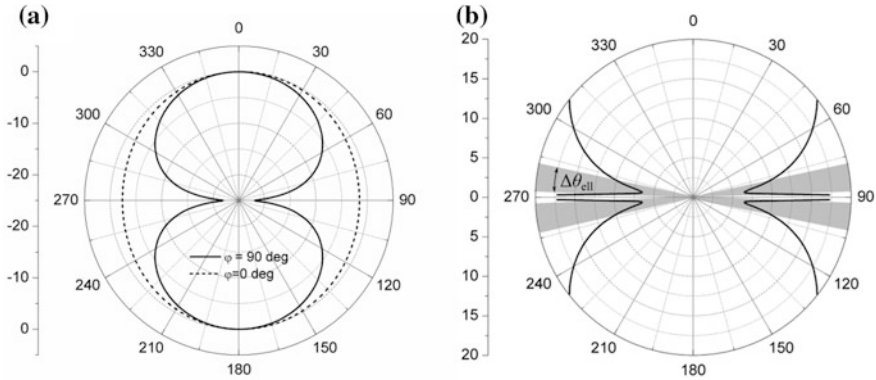


Fig. 2.10 Simulated **a** normalized radiation pattern and **b** axial ratio in the yz -plane of a lossless EC-SRR at the second resonance (with $c + d = 2.5$ mm). The low axial ratio (≤ 10 dB) region is depicted in grey

the EC-SRR at the second resonance is expected to be much lower than the quality factor of the same particle at the fundamental resonance. Specifically, doubling the antenna size in terms of wavelengths involves an increase of 8 times in the minimum radiation quality factor, since it depends upon the third power of the electric length of the antenna. However, these values should be considered only as qualitative, since very few antennas actually approach the lower bound of the radiation quality factor calculated on the basis of their size. Unfortunately, an analytical prediction of the EC-SRR quality factor at the second resonance is not straightforward. In fact, though a series RLC circuit model can be used to describe the particle behavior in terms of impedance (see Fig. 2.7a), no closed expressions linking the values of L and C to the geometrical values (r_0 , c , d) are known, unlike in the case of the first resonance. For this reason, the values presented in this work will be merely based on EM simulations, i.e., on the simulated half-power bandwidth $FBW = 2/Q$ when conjugate matching is obtained. For the lossless structure simulated in this section, the value of the fractional bandwidth is $FBW = 11.5\%$, corresponding to a radiation quality factor of $Q_{\text{rad}} = 17$. For comparison, Eq. (1.2) provides a lower bound of $Q_{\text{rad}} \geq 7.3$ (given that $r_{\text{ext}} = r_0 + c + d/2 = 37.5$ mm and $f_0 = 1$ GHz), which is sensibly smaller than the value found in our case. Even though the EC-SRR antenna does not approach the Gustafsson limit, its radiation quality factor is similar to that of a small planar rectangular (with a length-to-width ratio around unity) dipole antenna of the same size, and much lower as compared to small thin dipole antennas [14, 15].

Unlike in the case of working at the first resonance, the EC-SRR antenna at the second resonance can provide the bandwidth required for many applications, even outside the context of RFID, including wireless communication systems. A design example in the 900 MHz ISM band is described at Sect. 3.3, with the aim of providing experimental validation to the analysis carried out in this chapter, and to demonstrate the utility of the proposed antenna design.

2.3 Non-bianisotropic Split Ring Resonator (NB-SRR)

The non-bianisotropic split ring resonator was first proposed in [16] in order to avoid cross-polarization effects, which affect the behavior of many resonators (e.g., the EC-SRR), while maintaining uniplanar geometry. The topology of the resonator, along with a sketch of the electric current and charge distribution at the first and second resonance, is represented in Fig. 2.11. The non-bianisotropy in the particle response arises from the inversion symmetry with regard to its geometrical center, which ensures an exact cancellation of i) the tangential electric dipole generated at the first resonance and ii) the axial magnetic dipole generated at the second resonance, when uniform external excitations (such as plane waves) are considered. This is because both rings are identical, and the current/charge impressed in one ring presents the same amplitude of the current in the other ring. This is also true, though not formally exact, when the particle is excited as an antenna, i.e., through a differential port located in a cut opened in one of the rings, provided that the coupling between rings is strong, so that the current amplitudes in both rings are equal to i_0 . The absence of the cross-polarization terms in the polarizability tensor represents the most important difference between NB-CSRR and EC-SRR behavior, being their electrical sizes and their equivalent circuit models fundamentally equal [3]. Hence, the radiation resistance R_{rad} of the NB-SRR at the first and second resonance can be approximated by (2.8) and (2.36), respectively. Similarly, expressions (2.25) and (2.46) can be used to evaluate the loss resistance R_{loss} at the first and second resonance, respectively, along with expressions (2.26) and (2.47) for the radiation efficiency. On the other hand, the cross-polarization level $XPOL_{\text{max}}$ of the radiated fields is expected to be much lower (ideally zero), at both resonances, as compared to the EC-SRR, due to the absence of cross-polarization. Another expected characteristic of the NB-SRR radiation pattern at the second resonance is that the electric dipole moment is not oriented along the y-axis, as it happens in the case of the EC-SRR. In fact, due to

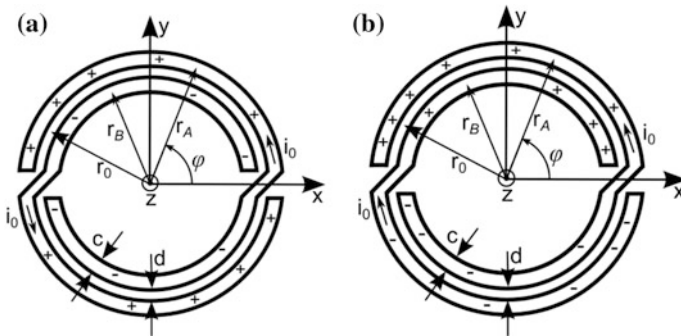


Fig. 2.11 Topology and theoretical current/charge distribution of the NB-SRR at the **a** first and **b** second resonance

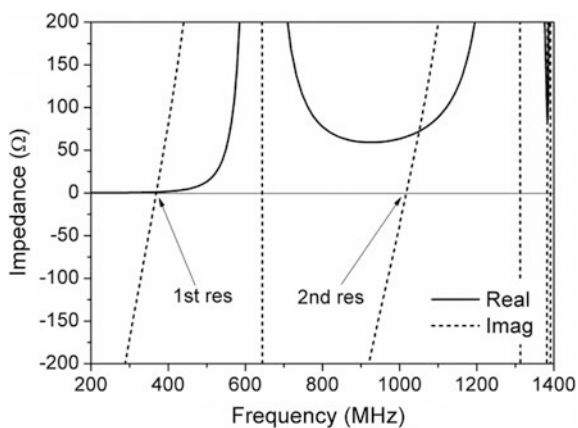
the NB-SRR topology, the ring center is not positioned at $\varphi = 0$, because the inner part of the ring is shorter than the outer part (the difference is increased when the $c + d$ is increased). Therefore, the ring center is shifted few degrees towards positive values of φ , and so the position of i_0 , depending primarily on the relationship between r_B and r_A . The ring center angle φ_0 is well approximated by the expression $\varphi_0 \approx \pi/2 \cdot (1 - r_B/r_A)$, or, alternatively, $\varphi_0 \approx \pi(c + d)/(2r_0 + c + d)$, provided that the cut width is greater than the distance $c + d$. As a result, the electric dipole moment is also expected to be rotated anti-clockwise of the same angle φ_0 with respect to the y -axis.

In order to confirm the behavior detailed above, a lossless NB-CSRR without substrate was simulated by means of *Agilent Advanced Design System (ADS)*. The values of the geometrical parameters r_0 , c and d are the same as in the case of the EC-SRR simulated in the previous section ($r_0 = 35.25$ mm, $c = 2$ mm, $d = 0.5$ mm, cut width 5 mm), so that the response of the structures can be compared. The differential port is placed at the position $\varphi_0 = 0.197$ (6°), which was calculated using the expression above, and corresponds to the ring center.

The simulated input impedance of the NB-SRR is depicted in Fig. 2.12: the analogy with the EC-SRR impedance (Fig. 2.7a) in all the frequency range is evident. The most relevant difference is that the radiation resistance of the NB-SRR at the second resonance (63Ω) is slightly smaller as compared to the EC-SRR (73Ω), due to the slightly different charge distribution (which is not treated in this work).

The radiation diagrams at the first (0.362 GHz) and second (1.016 GHz) resonance are shown in Fig. 2.13. The cut planes ($\theta = 90^\circ$, $\varphi = 6^\circ$) at the first resonance and ($\varphi = 96^\circ$, $\varphi = 6^\circ$) at the second resonance correspond to the E -plane and the H -plane, respectively. The simulated patterns confirm that the main difference between the patterns of the EC-SRR and the NB-CSRR is the absence of cross-polarization in the latter, while the directivity of the two particles are very similar (the NB-SRR provides $D_0 = 2$ dBi and $D_0 = 2.8$ dBi at the first and second resonance, respectively).

Fig. 2.12 Simulated input impedance of a lossless NB-SRR. Notice the analogy with the behavior of a EC-SRR of the same dimensions (see Fig. 2.7a)



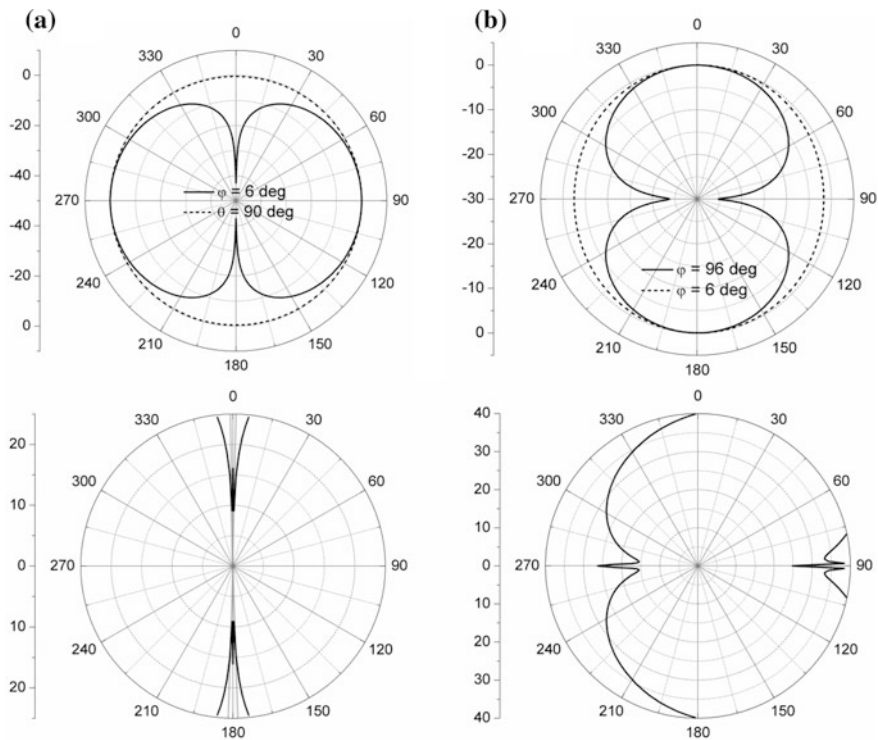


Fig. 2.13 Simulated normalized radiation pattern (*top*) and axial ratio in the $\phi = 96^\circ$ plane (*bottom*) of a lossless NB-SRR at the **a** first resonance and **b** second resonance. Notice that, due to the non-bianisotropy, the low-axial ratio (≤ 10 dB) region is practically inexistent

2.4 Complementary Particles (EC-CSRR, NB-CSRR): Free-Space and On-Metal Radiation

When a planar particle is replaced by its complementary screen, i.e., an unbounded, very thin and perfectly conductive sheet where the particle has been subtracted forming a slot, the complementary particle is obtained. For example, the complementary split ring resonator (CSRR), proposed in [17] as a means to obtain negative permittivity propagating structures, was obtained as the complementary screen of the EC-SRR (Fig. 2.14). This transformation can be applied to any planar particle, and allows obtaining equivalent structures which may be, in certain situations (e.g., when radiating over metallic surfaces), more convenient than the initial particle. As it is well known from the concept of duality and complementarity in electromagnetism [18, 19], the fields associated to a planar particle and its complementary screen are directly related. Specifically, being $F = (E, H)$ the solution for the electromagnetic field generated by a particle, the field $F' = (E', H')$ associated to its complementary screen in one half-space (delimited by the screen) is defined by

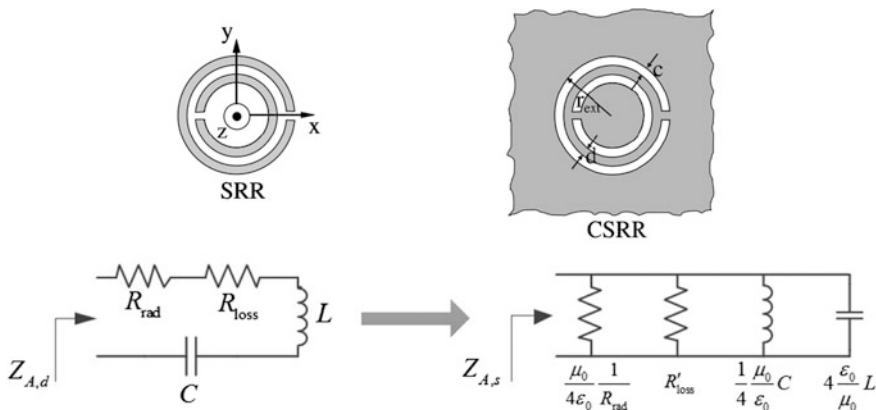


Fig. 2.14 Construction of the CSRR as the complementary screen of the EC-SRR (metal is depicted in grey) (*top*). Adapted with permission from [3]. Transformation of the equivalent circuit model, as seen from the center of the external ring (*bottom*)

$$F' = (E', H') = (-\sqrt{\mu/\varepsilon} \cdot H, \sqrt{\varepsilon/\mu} \cdot E), \quad (2.51)$$

while, due to the boundary conditions in the perfectly conductive screen and to the symmetry of the problem, the solution in the other half-space is $-F'$. It directly follows from duality that, in one side of the screen, the CSRR produces an axial electric dipole moment at the first resonance and a tangential magnetic dipole moment at the second resonance (of course, due to bi-anisotropy, each resonance actually generates both electric and magnetic moments). Equivalently, the CSRR can be seen as a magnetic current loop and a magnetic dipole at the first and second resonance, respectively. Another direct consequence of duality is that the radiation diagram of the complementary screen in an unbounded medium is the same as the radiation diagram of the particle, but the magnetic and electric field orientations are interchanged, and therefore the polarization is rotated [18]. Other far-field characteristics, such as the axial ratio, are maintained in the transformation.

As it was found by Booker in [18], duality also relates the driving impedance of a planar antenna to that of its complementary screen, namely:

$$Z_d Z_s = \frac{Z_0^2}{4} \quad (2.52)$$

where Z_d and Z_s are the impedances of the lossless particle and its complementary screen, respectively, and Z_0 is the impedance of free-space. From (2.52) it can be deduced that the admittance of the complementary particle is proportional to the impedance of the original particle, thus suggesting that a transformation from series to shunt occurs in the equivalent circuit model of the complementary particle around resonance. In fact, as it is well known in slot antenna theory, the radiated power is dependent upon the equivalent magnetic current, which corresponds to the

voltage applied to the slot at a certain position. Equation (2.52) allows obtaining the radiation conductance G_{rad} of the CSRR (or the NB-CSRR) directly from the previous expressions of the EC-SRR radiation resistance (Sects. 2.1 and 2.2), assuming that the particle is driven from the central position ($\varphi = 0$). At the first resonance, the radiation conductance of the ideal CSRR is found to be

$$G_{\text{rad}} = \frac{32}{3} \frac{\pi^5}{Z_0} \left(\frac{r_0}{\lambda_0} \right)^4, \quad (2.53)$$

while at the second resonance the value is

$$G_{\text{rad}} = \frac{512}{27} \frac{\pi}{Z_0} \left(\frac{r_0}{\lambda_0} \right)^2. \quad (2.54)$$

The values of the transformed shunt inductance and capacitance for the CSRR equivalent circuit model can be deduced by applying the Booker formula (2.52), obtaining the relations exposed in Fig. 2.14. It is easy to show that the radiation quality factor maintains in the transformation.

As said above, the complementary screen is an ideal structure which cannot exist in practice, so that, in many cases, the principle represents an approximation. First, the Babinet's principle does not take losses into account. When finite conductivity materials (such as copper) are used, a certain amount of ohmic losses is introduced, which is in general different from the amount of losses introduced by the same material in the original particle. Several studies [20–23] shown that there is no principle relating the total losses introduced in a resonator to the losses introduced in its complementary counterpart, and only approximated expressions depending upon the slot geometry can be obtained [22]. Therefore, the antenna efficiency is in general not maintained when passing to the complementary screen of a lossy resonator (an analytical calculation of the losses associated to the CSRR is very complex, and will not be treated in this work). In addition, the Babinet's principle requires the complementary screen to be infinitely extended and to radiate in an unbounded medium. In practice, the complementary antenna is limited in size, and it often radiates over/near other bodies, such as dielectrics or ground planes. Nonetheless, in many practical cases, the principle can still be considered as a good approximation, and remains a very useful guideline to understand the impedance and far-field behavior of slot antennas. For example, when the size of the surrounding metal sheet approaches the value of $\lambda_0/2\pi$ [18], a further size increase has little influence on the impedance of the antenna.

Concerning ground planes, they are sometimes intentionally placed below the complementary structure to confine its radiation to one half-space. In these cases, their distance can be properly adjusted (ideally to the distance of $\lambda_0/4$) to minimize the reactive loading thrown across the center of the slot antenna, and therefore to maintain the resonant frequency and the radiation pattern virtually unaltered. However, in on-metal UHF-RFID tag design, the ground plane is represented by the

metallic surface of the object, so that the distance from the radiating particle is equal to the tag thickness, which is supposed to be much smaller than $\lambda_0/4$ for obvious practical reasons. Thus, substantial changes in the particle response are expected due to the vicinity of the metal plane, such effect increasing as the distance h_s between the particle and the ground decreases. According to image theory, in one half-space (delimited by the ground plane) the system is equivalent to a set of two parallel complementary screens, separated from a distance $2h_s$, with currents flowing in opposite directions. Therefore, a system of two coupled CSRRs separated by an electric wall is obtained. According to coupled resonators theory [13], this situation leads to a decrease of the resonance frequency, with respect to the uncoupled CSRR, when the coupling between resonators is electric, and to an increase of the resonant frequency when the coupling is magnetic. As said above, the CSRR at first resonance produces a strong axial electric dipole moment, thus involving an electric coupling with the resonator image. For this reason, the first resonant frequency is lowered by the presence of a ground plane. On the other hand, it can be deduced that the second resonant frequency of the CSRR is raised by the presence of a ground plane, being basically a magnetic resonance. In both cases, the ground plane sensibly reduces the antenna radiation efficiency, due to several reasons. First, since the particle radiates only in one half-space, its radiation conductance G_{rad} is halved [18]. Moreover, the metal plane introduces an additional capacitance, as seen from antenna the input port (further increased when high-permittivity dielectric substrates are used), which involves an increase of the electric currents exciting the particle for a given applied port voltage, thus increasing the ohmic losses in the plane of the particle. Additional losses mechanisms include the ohmic losses on the metal plane, and dielectric losses (when a dielectric substrate is used). From the Poynting theorem, the latter can be evaluated according to

$$P_{\text{loss,die}} = \omega_0 \epsilon_0 \epsilon_r \tan \delta \iiint_V |E|^2 dV, \quad (2.55)$$

where ϵ_r and $\tan \delta$ are the substrate relative permittivity and loss tangent, respectively, E is the electric field evaluated in the volume V between the particle and the ground plane. Dimensional analysis suggests that dielectric losses in (2.55) tend to increase as the distance h_s from the metal plane decreases, for a given voltage applied to the slot.

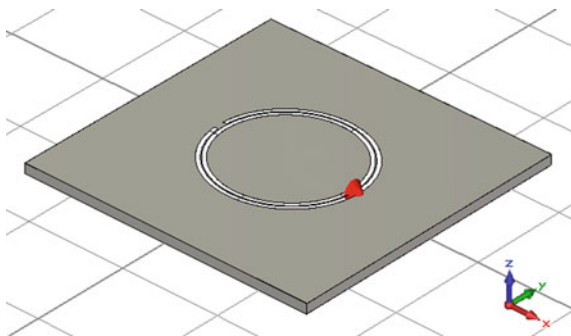
The radiation pattern of the CSRR in the radiating half-space is not substantially modified by the presence of the metal plane, provided that the electric field distribution along the slot (or, equivalently, the magnetic current distribution) maintains roughly unaltered (of course, 3 dB are added to the directive gain because the power is radiated in one half-space). On the other hand, as it was deduced by Booker, important modifications of the radiation pattern of a complementary antenna come from the finite dimensions of its screen, especially in the directions of the screen plane ($\theta = 90^\circ$), where, due to symmetry, no radiation is possible.

However, short-circuiting the screen edges to the ground plane is an effective way to avoid this effect, even when the metal surroundings of the particle are small. In this case, the boundary conditions allow exciting the structure by a plane wave coming from the direction $\theta = 90^\circ$, with electric field orientated in the z -direction, as in the case of an infinitely extended complementary screen. Technically, such antenna can be classified as a cavity-backed slot antenna, since the slot is boxed in a metallic cavity. It is known that the resonant modes in the cavity might affect the electric field distribution on the slot [24], and consequently the radiation pattern. We observed that the boxed CSRR antenna, excited with a voltage across the center of the outer ring slot (see Fig. 2.15), maintains a radiation pattern similar (in one half-space) to that of the unbounded complementary screen, even for very small distances from the metal plane (Fig. 2.17).

The behavior described above was verified by means of electromagnetic simulations, which also provided an estimation of the resonance split and the radiation efficiencies for different distances (5, 2, 1.27 mm, no metal plane) of the CSRR over the metal plane. To this end, the commercial software *CST Microwave Studio* was used. The CSRR was etched on an infinitely extended screen made of (a) perfectly conductive material (lossless case) and (b) copper (lossy case), with thickness $h = 35 \mu\text{m}$, and excited with a differential port placed across the slot at the position $\varphi = 0$. In order to compare the impedance response, the simulated CSRR has the same dimensions as the EC-SRR simulated at Sect. 2.2 ($r_0 = 35.25 \text{ mm}$, $c = 2 \text{ mm}$, $d = 0.5 \text{ mm}$). In the cases which consider the presence of a ground plane below the resonator, the screen containing the CSRR was cut with lateral dimensions of $150 \text{ mm} \times 150 \text{ mm}$, and the four sides of the square were connected to ground by means of vertical copper walls (with thickness equal to h). The ground was defined by forcing the boundary condition $E_t = 0$ (where E_t is the electric field tangential to the plane), which describes a lossless and infinitely extended ground plane.

The simulated input antenna impedance for different cases is depicted in Fig. 2.16. As expected, the frequency split associated to the presence of the ground plane is evident. It is interesting to note that, even for very small distances from the ground plane ($h_s = 1.27 \text{ mm}$), the impedance response of the CSRR clearly shows its resonances, thus suggesting that the particle behavior is not strongly affected by

Fig. 2.15 Finite size CSRR antenna short-circuited to the ground plane. Metal is depicted in grey; the ground plane is represented by the grid. The excitation port is represented by the red triangle



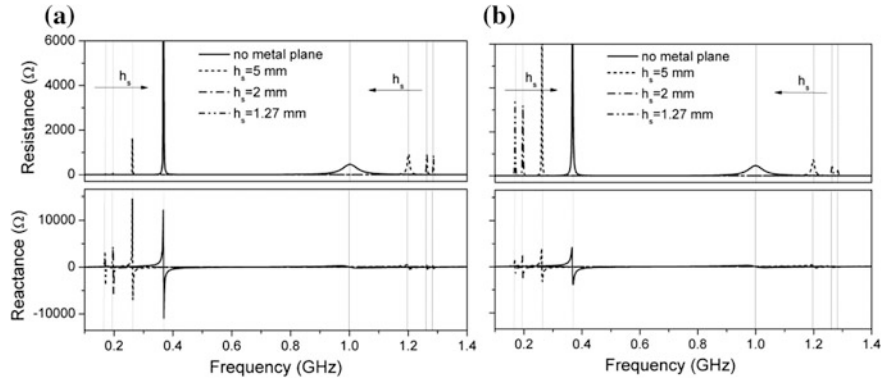


Fig. 2.16 Simulated input impedance of a **a** lossless and **b** lossy (etched on a copper layer) CSRR at different distances over an infinitely extended ground plane (first resonances are marked in *light grey*, second resonances in *dark grey*)

Table 2.2 Simulated values for the first and second resonant frequencies of the boxed CSRR over an ideal ground plane

	f_1 (GHz)	f_2 (GHz)	η_{rad1} (%)	η_{rad2} (%)
No ground	0.37	1	45	98
$h_s = 5$ mm	0.26	1.2	6	77
$h_s = 2$ mm	0.2	1.26	2	46
$h_s = 1.27$ mm	0.17	1.28	<1%	30

the ground plane. In case no ground plane is present, the first (0.37 GHz) and second (0.99 GHz) resonances of the CSRR agree very well with the resonant frequencies of an EC-SRR of the same dimensions (see Fig. 2.7). The radiation conductance G_{rad} calculated by using (2.53) and (2.54) for the first and second resonances, respectively, shows good agreement with the simulated values in the unbounded lossless case, as expected from duality. The theoretical/simulated values are 3.1×10^{-5} S/ 4.2×10^{-5} S at the first resonance, and 2.2×10^{-3} S/ 2.1×10^{-3} S at the second resonance.

Equation (2.53) and (2.54) were also applied to predict the radiation conductance when the radiation is confined by the ground plane, taking into account that the results must be halved, since radiation occurs only in one half-space. In this case, however, the theoretical prediction is not as accurate as in the unbounded case, and only provides a rough approximation.

As can be seen in Fig. 2.16, ohmic losses associated to copper do not introduce changes in the resonant frequencies. In such a lossy case, one of the main concerns is the radiation efficiency, which can be severely affected as the distance from the ground plane is made very small. As illustrated in Table 2.2, the simulated values of the radiation efficiency decrease as the value of h_s is reduced. At the first resonance, the efficiency quickly falls to very small values, due to the combined effect of the electrical size reduction (the first resonance is lowered down to half its value) and the

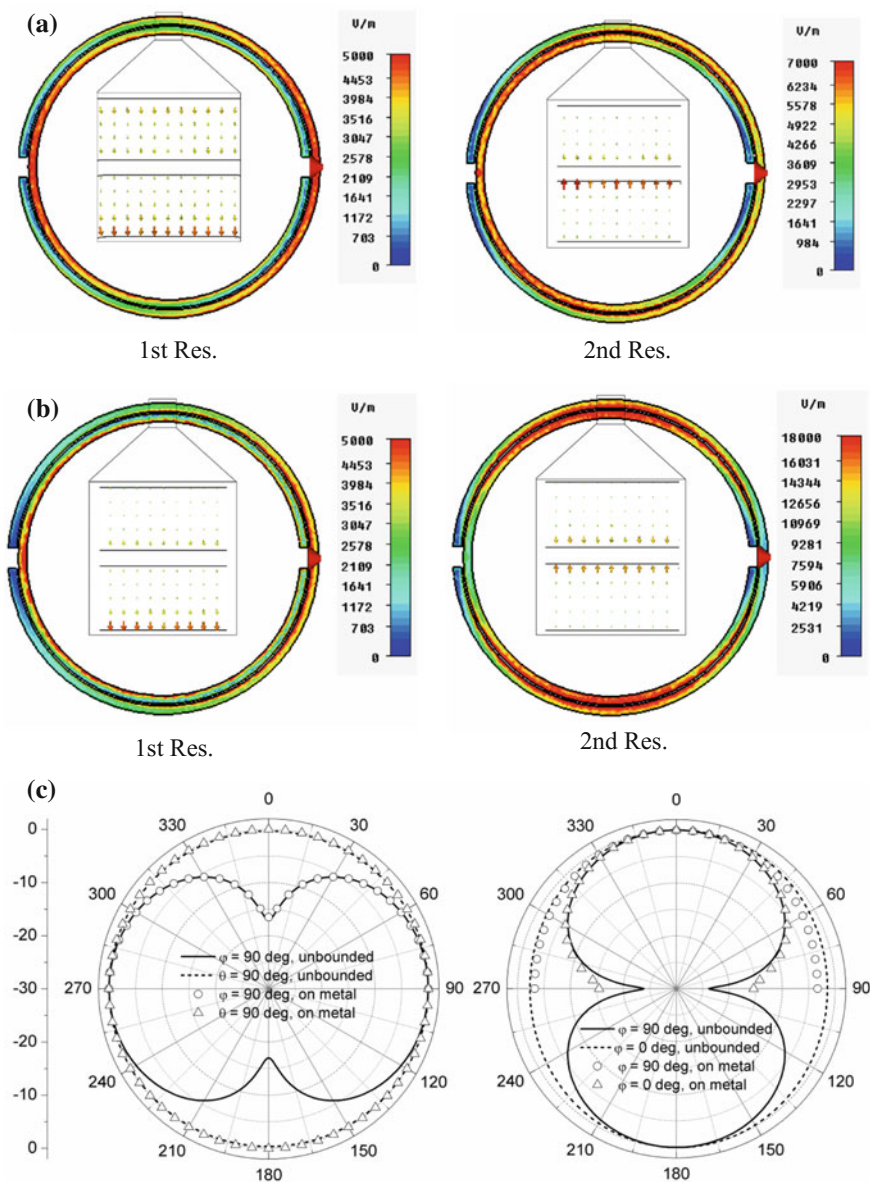


Fig. 2.17 Amplitude of the electric field tangential to the slot of the **a** unbounded CSRR and **b** CSRR boxed on a ground plane (at a distance $h_s = 1.27$ mm). A zoom of the E -field vector in the slot at the position $\varphi = 90^\circ$ is also represented. **c** Radiation pattern at the first and second resonance (left and right, respectively)

additional losses arising from the vicinity of the ground plane. On the other hand, the results at the second resonance are encouraging even for the smallest value of $h_s = 1.27 \text{ mm}$ ($\lambda/185$), where $\eta_{\text{rad}} = 30\%$ is predicted. It is worth mentioning that no substrate has been considered so far. Obviously, a dielectric substrate may be necessary in many practical cases, due to its structural function. Moreover, when designing an UHF-RFID tag based on this resonance, one might want to reduce lateral dimensions, which have been increased by the presence of the metal plane (a $100 \text{ mm} \times 100 \text{ mm}$ tag would result when working at 915 MHz without adding any substrate, so that the resulting tag area would be significantly larger than average), and this can be accomplished by properly choosing the permittivity of the substrate. However, as mentioned before, the substrate may cause an important reduction of the radiation efficiency, so that a careful tradeoff between tag dimensions and read range is necessary at the tag design stage.

Let us now check the electric field distribution and the radiation pattern of the CSRR (Fig. 2.17) when boxed on a ground plane. The simulation results suggest that, even when the distance from the ground is small (1.27 mm), the field distribution on the slot is similar to that of the ideal CSRR. Notice that, due to duality, the proximity effects encountered in the EC-SRR are also replicated in the electric field distribution (or, equivalently, in the magnetic current density) on the slot. As a result, the radiation pattern (in the upper half space) is also very similar (Fig. 2.7c).

In conclusion, although the ground plane lowers the radiation efficiency of the CSRR, it is actually interesting to explore this solution for the design of UHF-RFID tags with low-profile and acceptable read range, in light of the novelty that this kind of design represents over the state of the art. In the next chapter, an on-metal UHF-RFID tag based on a NB-CSRR working at the second resonance will be presented, along with the design concepts and the measured read range.

References

1. Harrington RF (1964) Theory of loaded scatterers. In: Proceedings of the institution of electrical engineers, pp 617–623
2. Marqués R, Medina F, Rafii-El-Idrissi R (2002) Role of bianisotropy in negative permeability and left-handed metamaterials. *Phys Rev B* 65:144440
3. Marques R, Martin F, Sorolla M (2008) *Metamaterials with negative parameters*. Wiley-Interscience, Hoboken, N.J.
4. Murgatroyd PN (1989) Calculation of Proximity losses in multistranded conductor bunches. *IEE Proc Sci Meas Technol* 136:115–120
5. Orfanidis SJ (2002) *Electromagnetic waves and antennas*. Rutgers University, New Brunswick, NJ
6. Jackson JD (1962) *Classical electrodynamics*, vol 3. Wiley, New York
7. Pozar DM (2009) *Microwave engineering*. Wiley, New York
8. Marques R, Mesa F, Martel J, Medina F (2003) Comparative analysis of edge- and broadside-coupled split ring resonators for metamaterial design—theory and experiments. *IEEE Trans Antennas Propag* 51:2572–2581
9. Balanis CA (2005) *Antenna theory: analysis and design*, 3rd edn. Wiley, Hoboken, NJ

10. Pozar DM (2009) New results for minimum Q, Maximum gain, and polarization properties of electrically small arbitrary antennas. In: European conference on antennas and propagation, pp 1914–1917
11. Zamora G, Paredes F, Herraiz-Martinez FJ, Martín F, Bonache J (2013) Bandwidth limitations of ultra high frequency-radio frequency identification tags. *IET Microw Antennas Propag* 7:788–794
12. García-García J, Martín F, Baena JD, Marques R, Jelinek L (2005) On the resonances and polarizabilities of split ring resonators. *J Appl Phys* 98 (Aug 1 2005)
13. Hong J-S, Lancaster MJ (2001) Microstrip filters for RF/microwave applications. Wiley, New York
14. Gustafsson M, Sohl C, Kristensson G (2009) Illustrations of new physical bounds on linearly polarized antennas. *IEEE Trans Antennas Propag* 57:1319–1327
15. Mohammadpour-Aghdam K, Faraji-Dana R, Vandenbosch GA, Radiom S, Gielen GG (2011) Physical bound on Q factor for planar antennas. In: European microwave conference (EuMC), pp 250–252
16. Marqués R, Baena J, Martel J, Medina F, Falcone F, Sorolla M, Martín F (2003) Novel small resonant electromagnetic particles for metamaterial and filter design. *Proc ICEAA* 3:439–442
17. Falcone F, Lopetegui T, Laso M, Baena J, Bonache J, Beruete M, Marqués R, Martín F, Sorolla M (2004) Babinet principle applied to the design of metasurfaces and metamaterials. *Phys Rev Lett* 93:197401
18. Booker HG (1946) Slot aeriels and their relation to complementary wire aeriels (Babinet's principle). *J Inst Electr Eng Part IIIA Radiolocation* 93:620–626
19. Deschamps GA (1959) Impedance properties of complementary multiterminal planar structures. *IRE Trans Antennas Propag* 7:371–378
20. Lang K (1973) Babinet's principle for a perfectly conducting screen with aperture covered by resistive sheet. *IEEE Trans Antennas Propag* 21:738–740
21. Senior T (1977) Some extensions of Babinet's principle in electromagnetic theory. *IEEE Trans Antennas Propag* 25:417–420
22. Hansen R (1998) Slot antenna in a resistive screen. *IEEE Trans Antennas Propag* 46: 1028–1031
23. Yoshitomi K (2001) Radiation from a slot in an impedance surface. *IEEE Trans Antennas Propag* 49:1370–1376
24. Vallecchi A, Gentili GB (2007) Microstrip-fed slot antennas backed by a very thin cavity. *Microwave Opt Technol Lett* 49:247–250
25. Nikitin PV, Lam S, Rao K (2005) Low cost silver ink RFID tag antennas. In *IEEE Antennas Propag Soc Int Symp*, pp 353–356, 2005
26. Pongpaibool P (2012) A study of cost-effective conductive ink for inkjet-printed RFID application. In: International symposium on antennas and propagation (ISAP), Nagoys, pp 1248–1251
27. Zuffanelli S, Zamora G, Aguilà P, Paredes F, Martín F, Bonache J (2015) On the radiation properties of split-ring resonators (SRRs) at the second resonance. *IEEE Trans Microw Theory Tech* 63(7):2133–2141

Antenna Design Solutions for RFID Tags Based on
Metamaterial-Inspired Resonators and Other Resonant
Structures

Zuffanelli, S.

2018, XIII, 149 p. 87 illus., 39 illus. in color., Hardcover

ISBN: 978-3-319-62029-9